Comparison of the structural and electrochemical properties of layered Li[Ni$_x$Co$_y$Mn$_z$]O$_2$ (x = 1/3, 0.5, 0.6, 0.7, 0.8 and 0.85) cathode material for lithium-ion batteries

Hyung-Joo Noh [a], Sungjune Youn [a], Chong Seung Yoon [b,*], Yang-Kook Sun [a,*]

[a] Department of WCU Energy Engineering, Hanyang University, Seoul 133-791, South Korea
[b] Department of Materials Science and Engineering, Hanyang University, Seoul 133-791, South Korea

HIGHLIGHTS

► Li[Ni$_x$Co$_y$Mn$_z$]O$_2$ were synthesized via a coprecipitation method.
► The electrochemical and thermal properties are dependent on their compositions.
► Increasing Ni content raises the capacity whereas increasing Mn content improves safety.

GRAPHICAL ABSTRACT
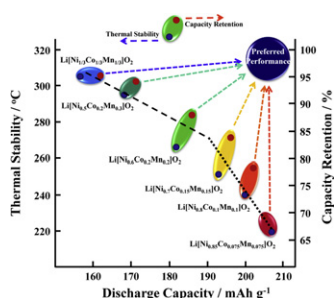
ABSTRACT

In this study we report the effects of the Ni content on the electrochemical properties and the structural and thermal stabilities of Li[Ni$_x$Co$_y$Mn$_z$]O$_2$ (x = 1/3, 0.5, 0.6, 0.7, 0.8 and 0.85) synthesized via a coprecipitation method. The electrochemical and thermal properties of Li[Ni$_x$Co$_y$Mn$_z$]O$_2$ are strongly dependent on its composition. An increase of the Ni content results in an increase of specific discharge capacity and total residual lithium content but the corresponding capacity retention and safety characteristics gradually decreased. The structural stability is related to the thermal and electrochemical stabilities, as confirmed by X-ray diffraction, thermal gravimetric analysis, and differential scanning calorimetry. Developing an ideal cathode material with both high capacity and safety will be a challenging task that requires precise control of microstructure and physico-chemical properties of the electrode.

1. Introduction

Rechargeable lithium-ion batteries have become a common power source for portable electronic devices due to their high energy density, high voltage, and long cycle life. Further improvement of the energy density has enabled lithium-ion batteries to be used for automobile applications such as plug-in hybrid vehicles (PHEVs) and electric vehicles (EVs). However, the widespread use of these batteries in the automobile industry requires further improvements of their energy density and safety. The energy densities of lithium-ion batteries have increased by only a factor of 2–3 times since their introduction by Sony in 1991 as the gravimetric energy density has increased from 98 to 185 Wh kg^{-1} and the volumetric energy density has increased from 220 to 620 Wh L^{-1}. The techniques to optimize the cell design to maximize the packing density

---

* Corresponding authors.
E-mail addresses: csyoon@hanyang.ac.kr (C.S. Yoon), yksun@hanyang.ac.kr (Y.-K. Sun).

and improve the battery structure have advanced to a point where there is no room left for improvement. Hence, the development of new cathode materials with a high capacity and high level of safety is indispensable for high performance lithium-ion batteries [1–4]. Great efforts have been made toward the synthesis of lithium transition metal oxide materials such as $Li[Ni_xCo_{1-2x}Mn_x]O_2$ [5–9] and $Li[Ni_{1-x-y}Co_xMn_y]O_2$ [10–14]. Among these layered materials, $Li[Ni_{1/3}Co_{1/3}Mn_{1/3}]O_2$ has already been commercialized for automobile applications due to its high capacity and outstanding safety characteristics. However, its capacity of 155 mAh g^{-1} is quite low for use in next-generation EVs applications [15]. $Li[Ni_{1-x-y}Co_xMn_y]O_2$ materials $(1 - x - y \geq 0.5)$ deliver higher capacities than $Li[Ni_{1/3}Co_{1/3}Mn_{1/3}]O_2$ due to the higher Ni content which is the main active redox species (Ni^{2+} ⇆ Ni^{4+}) in the host structure. The thermal stability of $Li[Ni_{1-x-y}Co_xMn_y]O_2$ is also directly related to the Ni content. In other words, the relationship between capacity and safety is a trade-off. It is well known that Ni provides a high capacity but poor thermal stability, while Mn maintains an outstanding cycle life and safety. Also, Co offers increased electronic conductivity resulting in an excellent rate capability. Hence, the intrinsic properties of $Li[Ni_{1-x-y}Co_xMn_y]O_2$ materials strongly depend on the amounts of the metal ions (Ni, Co, Mn). However, the relationships between the compositions and the capacity and thermal stability in layered lithium metal oxides have not been systematically studied.

In this report, we intensively studied the effects of the transition metal composition on the electrochemical properties and the structural and thermal stabilities of $Li[Ni_xCo_yMn_z]O_2$ $(x:y:z = 1/3:1/3:1/3, 0.5:0.2:0.3, 0.6:0.2:0.2, 0.70:0.15:0.15, 0.8:0.1:0.1$ and $0.85:0.075:0.075$, hereafter defined as $x = 1/3, 0.5, 0.6, 0.7, 0.8$ and 0.85, respectively).

2. Experimental

Spherical $[Ni_xCo_yMn_z](OH)_2$ precursors $(x = 1/3, 0.5, 0.6, 0.7, 0.8$ and $0.85)$ were synthesized via the coprecipitation method [16]. The appropriate amounts of $NiSO_4 \cdot 6H_2O$, $CoSO_4 \cdot 7H_2O$, and $MnSO_4 \cdot 5H_2O$ were used as the starting materials for the synthesis of $[Ni_xCo_yMn_z](OH)_2$. An aqueous solution of $NiSO_4 \cdot 6H_2O$, $CoSO_4 \cdot 7H_2O$, and $MnSO_4 \cdot 5H_2O$ with a concentration of 2.0 mol L^{-1} was pumped into a continuously stirred tank reactor (CSTR, 4 L) under a N$_2$ atmosphere. Concurrently, a 4.0 mol L^{-1} NaOH solution (aq.) and the desired amount of NH$_4$OH solution (aq.) as a chelating agent were separately pumped into the reactor. The concentration of the solution, pH, temperature, and stirring speed of the mixture in the reactor were carefully controlled. The precursor powders were obtained through filtering, washing, and drying in a vacuum oven overnight. $Li[Ni_xCo_yMn_z]O_2$ $(x = 1/3, 0.5, 0.6, 0.7, 0.8$ and $0.85)$ were prepared by thoroughly mixing the precursor $[Ni_xCo_yMn_z](OH)_2$ with $LiOH \cdot H_2O$ followed by calcination at various temperatures for 15 h: 950 °C for $Li[Ni_{1/3}Co_{1/3}Mn_{1/3}]O_2$, 950 °C for $Li[Ni_{0.5}Co_{0.2}Mn_{0.3}]O_2$, 900 °C for $Li[Ni_{0.6}Co_{0.2}Mn_{0.2}]O_2$, 850 °C for $Li[Ni_{0.7}Co_{0.15}Mn_{0.15}]O_2$, 780 °C for $Li[Ni_{0.8}Co_{0.1}Mn_{0.1}]O_2$ and 750 °C for $Li[Ni_{0.85}Co_{0.075}Mn_{0.075}]O_2$. Powder X-ray diffraction (XRD, Rigaku, Rint-2000) using Cu Kα radiation was used to identify the crystalline phases of the prepared and cycled powders. The XRD data were obtained in the 2θ range of 10–80° with a step size of 0.03°. The lattice parameters of $Li[Ni_xCo_yMn_z]O_2$ were calculated using the Celref software by fitting the experimental XRD data to the rhombohedral structure. The morphologies of the prepared powders were observed using scanning electron microscopy (SEM, JSM-6340F, JEOL). The total residual lithium amounts were measured by titration method (T50, METTLER TOLEDO, Switzerland) in which the Li sources are believed to originate from LiOH and Li_2CO_3 since the Li_2CO_3 was also dissolved in water in a basic solution.

The cell consisted of a positive cathode and a lithium metal anode separated by a porous polypropylene film. Positive electrodes were prepared by blending $Li[Ni_xCo_yMn_z]O_2$ active materials, Super P carbon black, and polyvinylidene fluoride (85:7.5:7.5). The slurry was cast onto aluminum foil and dried at 110 °C for 10 h in a vacuum oven. The electrochemical characterizations were performed using a 2032 coin-type cell with a 1 M LiPF$_6$ solution in a ethylene carbonate (EC)-diethyl carbonate (DEC) mixture (1:1 volume ratio, PANAX ETEC Co. Ltd, Korea). Cycling tests were performed at a constant current with an upper cutoff voltage of 4.3 V at 25 °C and 55 °C. The DC electrical conductivity was measured by a direct volt–ampere method (CMT-SR1000, AIT Co.) in which disk samples was contacted with a four-point probe. For analysis by differential scanning calorimetry (DSC), the 2032 coin-type cells were fully charged to 4.3 V and opened in an Ar-filled dry room. After the remaining electrolyte was carefully removed from the surface of the electrode, the cathode materials were recovered from the current collector. A stainless steel sealed pan with a gold-plated copper seal was used to collect 3–5 mg samples. Measurements were performed in a DSC 200 PC (NETZSCH, Germany) at a temperature scan rate of 1 °C min^{-1}.

3. Results and discussion

Fig. 1 shows the X-ray powder diffraction patterns of the prepared $Li[Ni_xCo_yMn_z]O_2$ $(x = 1/3, 0.5, 0.6, 0.7, 0.8$ and $0.85)$ powders. All of the powders exhibited a well-defined layer structure based on a hexagonal a-NaFeO$_2$ structure with a $R\overline{3}m$ space group and no impurity phases. The clear peak splits in the (108)/(110) and (006)/(102) doublets were observed for all samples, indicating highly crystalline layer materials. The $I(003)/I(104)$ ratio indirectly indicates cation mixing between Li$^+$ and Ni^{2+} in the lithium layer. Usually, higher $I(003)/I(104)$ ratio shows increased cation mixing. The Ni^{2+} ions in the Li layer not only decrease discharge capacity but impede to Li$^+$ ionic diffusivity. Such structural disorders are known as a main cause for the poor electrochemical performance. As shown in Table 1, the intensity ratio of the (003)/(104) peaks decreased from 1.35 for $x = 1/3$ to 1.18 for $x = 0.85$ as the Ni content increased due to the similar ionic radii of Ni^{2+} (0.69 Å) and Li$^+$ (0.76 Å) [17]. Note that the $I(003)/I(104)$ ratio changes very little above $x = 0.7$, suggesting that the electrochemical performance may deteriorate for these compositions during extended cycling.

Fig. 2 shows the SEM images of the $Li[Ni_xCo_yMn_z]O_2$ $(x = 1/3, 0.5, 0.6, 0.7, 0.8$ and $0.85)$ powders. All of the powders had a spherical morphology with an average particle diameter of 10 μm. Each

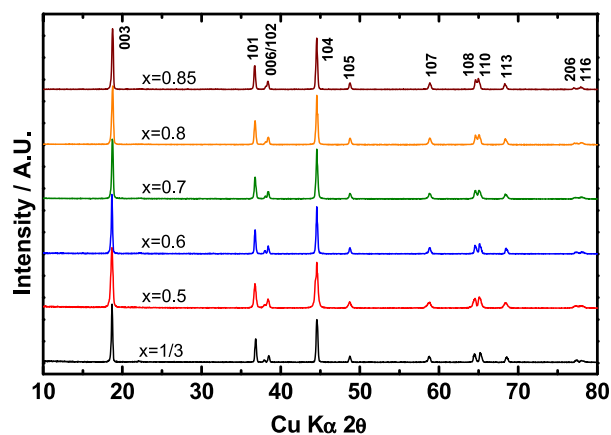**Fig. 1.** Powder XRD patterns of as-prepared $Li[Ni_xCo_yMn_z]O_2$ $(x = 1/3, 0.5, 0.6, 0.7, 0.8$ and $0.85)$.

Table 1
Intensity ratio $I(003)/I(004)$ of the Li[$Ni_xCo_yMn_z$]O_2 ($x = 1/3$, 0.5, 0.6, 0.7, 0.8 and 0.85).

	$I_{(003)}/I_{(104)}$
Li[$Ni_{1/3}Co_{1/3}Mn_{1/3}$]O_2	1.35
Li[$Ni_{0.5}Co_{0.2}Mn_{0.3}$]O_2	1.32
Li[$Ni_{0.6}Co_{0.2}Mn_{0.2}$]O_2	1.26
Li[$Ni_{0.7}Co_{0.15}Mn_{0.15}$]$O_2$	1.20
Li[$Ni_{0.8}Co_{0.1}Mn_{0.1}$]O_2	1.19
Li[$Ni_{0.85}Co_{0.075}Mn_{0.075}$]$O_2$	1.18

spherical secondary particle was composed of an agglomerate of primary particles with estimated particle sizes of 0.1–1.8 μm. The primary particle size decreased noticeably with increasing Ni content, which can be related with poor cycle life due to increased contact area with electrolyte.

It is well known that Li[$Ni_xCo_yMn_z$]O_2, especially with $x > 0.6$, readily reacts with air, resulting in the formation of Li_2CO_3 and LiOH on the cathode surface [18,19]. The formed LiOH reacts with $LiPF_6$ and generates acidic HF in the electrolyte. In addition, Li_2CO_3 gives rise to severe swelling upon storage at high temperatures, especially in the charged state [20]. Table 2 exhibits the total residual lithium amounts (LiOH and Li_2CO_3) on the cathode surfaces. The total residual lithium amount increased with increasing Ni content in Li[$Ni_xCo_yMn_z$]O_2 and increased drastically at Ni contents (x) above 0.7. For example, the residual lithium amount increased from 4908 ppm for Li[$Ni_{0.6}Co_{0.2}Mn_{0.2}$]O_2 to 11,054 ppm for Li[$Ni_{0.7}Co_{0.15}Mn_{0.15}$]$O_2$, which is difficult to use to fabricate a good electrode due to gelation of the cathode slurry caused by the increased pH. The Li[$Ni_{0.8}Co_{0.1}Mn_{0.1}$]O_2 and Li[$Ni_{0.85}Co_{0.075}Mn_{0.075}$]$O_2$ materials had even higher residual lithium amounts of 23,819 ppm and 26,542 ppm, respectively.

The fundamental electrochemical properties of the Li[$Ni_xCo_yMn_z$]O_2 ($x = 1/3$, 0.5, 0.6, 0.7, 0.8 and 0.85) powders were evaluated using a 2032 coin-type half-cell employing Li metal as the anode. Fig. 3a shows the initial charge–discharge curves of Li/Li[$Ni_xCo_yMn_z$]O_2 ($x = 1/3$, 0.5, 0.6, 0.7, 0.8 and 0.85) between 3.0 and 4.3 V at a constant current density of 20 mA g^{-1} (0.1 C-rate) and 25 °C. The initial discharge capacity of the Li[$Ni_xCo_yMn_z$]O_2 electrodes increased with increasing Ni content (x), which is the main redox species [20] with values of 206 mAh g^{-1} for $x = 0.85$, 203 mAh g^{-1} for $x = 0.8$, 194 mAh g^{-1} for $x = 0.7$, 187 mAh g^{-1} for $x = 0.6$, 175 mAh g^{-1} for $x = 0.5$ and 163 mAh g^{-1} for $x = 1/3$.

In order to clearly determine the different redox behaviors of the Li[$Ni_xCo_yMn_z$]O_2 electrodes, the charge and discharge curves with cycling were obtained and the corresponding differential capacity vs. voltage profiles ($dQ \ dV^{-1}$) are shown in Fig. 3b–f. At the first cycle, the Li/Li[$Ni_xCo_yMn_z$]O_2 ($x = 1/3$) cell exhibited redox peaks at around 3.76 V on charging and 3.72 V on discharging. However, a new oxidation peak around 3.64 V appeared with increasing Ni content. Furthermore, the Li/Li[$Ni_xCo_yMn_z$]O_2 ($x = 0.8$) cell showed four distinct redox peaks with a sharp oxidation peak at 3.62 V and several other secondary peaks (3.78 V, 4.04 V and 4.23 V) which appeared during charging due to the multiphase transitions of hexagonal to monoclinic (H1 → M), monoclinic to hexagonal (M → H2), and hexagonal to hexagonal (H2 → H3) [21,22]. The corresponding reduction peaks were present at 3.58 V, 3.72 V, 3.98 V, and 4.18 V. As the cycling proceeded, the redox peaks for the Li/Li[$Ni_xCo_yMn_z$]O_2 ($x = 1/3$) cell are very stable. However, the redox peaks changed to a more polarized state and shifted further apart with increasing Ni content (x). In particular, the oxidation peak at 3.62 V for the Li/Li[$Ni_xCo_yMn_z$]O_2 ($x = 0.8$) cell became smaller and moved to 3.76 V after 100 cycles. It has been reported that the rapid volume contraction during the structural transformation from H2 to H3 mostly affects the capacity fading of the Li[$Ni_xCo_yMn_z$]O_2 [21].

The lack of H2–H3 phase transition with decreasing Ni content indicates good reversibility of the Li[$Ni_xCo_yMn_z$]O_2 electrode, and is indeed reflected in the stability of host structure which well matched with smaller volume variation after cycling shown in Fig. 5. Hence, good cycling performance of the Ni-deficient Li[$Ni_xCo_yMn_z$]O_2 electrode is believed to be due mainly to suppression of the H2 + H3 transition. In addition, the reduction in the discharge voltage with cycling represented by the arrow indicates an increase of the internal resistance (IR). The extent of this IR drop increased with increasing Ni content.

Fig. 4 illustrates the discharge capacities vs. cycle number of the Li/Li[$Ni_xCo_yMn_z$]O_2 ($x = 1/3$, 0.5, 0.6, 0.7, 0.8 and 0.85) cells cycled between 3.0 and 4.3 V at 25 °C and 55 °C. The tests were performed at a constant current density of 100 mA g^{-1} (0.5 C-rate). As expected, the Li$^+$ intercalation stability of the materials increased with decreasing Ni content (x). For example, although Li[$Ni_{0.85}Co_{0.075}Mn_{0.075}$]$O_2$ delivered the highest discharge capacity of 208 mAh g^{-1}, it showed a rapid decrease of capacity, leading to a capacity retention of only 55.6% (100 mAh g^{-1}) after 100 cycles at 55 °C. By contrast, the Li$^+$ intercalation stability of the Ni-deficient Li[$Ni_{1/3}Co_{1/3}Mn_{1/3}$]O_2 was remarkably improved, showing a capacity retention of more than 92.4% while still maintaining a discharge capacity of 150 mAh g^{-1} over the same cycling period and temperature. The capacity retentions of the other Li[$Ni_xCo_yMn_z$]O_2 materials were 90.0%, 85.1%, 78.5% and 70.2% for x values of 0.5, 0.6, 0.7 and 0.8, respectively. As is well known, the poor Li$^+$ intercalation stability of Ni-rich Li[$Ni_xCo_yMn_z$]O_2 ($x \geq 0.7$) can result from the formation of a more stable spinel phase [22] or stable $Li_xNi_{1-x}O$ phase [23], leading to an increase of the interfacial resistance upon cycling. We believe that the enhanced capacity retention of Ni-deficient Li[$Ni_xCo_yMn_z$]O_2 ($x \leq 0.5$) results from not only its stable composition with increased Mn and reduced Ni concentrations but also its increased structural stability. In addition, the excess lithium on the particle surface shown in Table 2 is expected to accelerate the dissolution of the transition metals from the particle surface, leading to the capacity fading.

In order to investigate the structural stabilities of Li[$Ni_xCo_yMn_z$]O_2 ($x = 1/3$, 0.5, 0.6, 0.7, 0.8 and 0.85), the variations of the lattice parameters (a and c) and the unit cell volumes of the materials before and after 100 cycles at 25 °C were calculated and the results are shown in Fig. 5. These data clearly show that the variations of the lattice parameters and unit cell volume increase with increasing Ni content. Li[$Ni_{0.85}Co_{0.075}Mn_{0.075}$]$O_2$ suffers from a dramatic increase of the lattice parameters and the cell volume while the values for the cycled Li[$Ni_{1/3}Co_{1/3}Mn_{1/3}$]O_2 electrode remained nearly constant compared to the other electrodes. Note that there is a linear relationship of the difference of the lattice parameters and volume expansion with respect to the composition for $x = 1/3 - 0.85$. However, the variation of the difference deviated from $x = 0.7$ upward, indicating that the cycled electrode suffered increasingly higher volume expansion. The increased volume expansion partially contributed to the abrupt decrease of the capacity retention above $x = 0.7$.

To complement the XRD data on the structural stabilities, transmission electron microscopy (TEM) was carried out on the electrodes for 100 cycles with the upper cutoff voltage of 4.3 V at 55 °C. Although the XRD data in Fig. 5 shows a clear trend in the expansion of the unit cell during cycling, no distinguishable change in the overall crystal structure of the cycled electrode was detected by XRD (not shown here). In order to observe fine structural changes on individual primary particles, the Li[$Ni_{0.85}Co_{0.075}Mn_{0.075}$]$O_2$ which showed the largest capacity fade during cycling was first examined with TEM. A bright field image shown in Fig. 6a indicates the primary particle size was relatively small for Li[$Ni_{0.85}Co_{0.075}Mn_{0.075}$]$O_2$ so that the particles surface
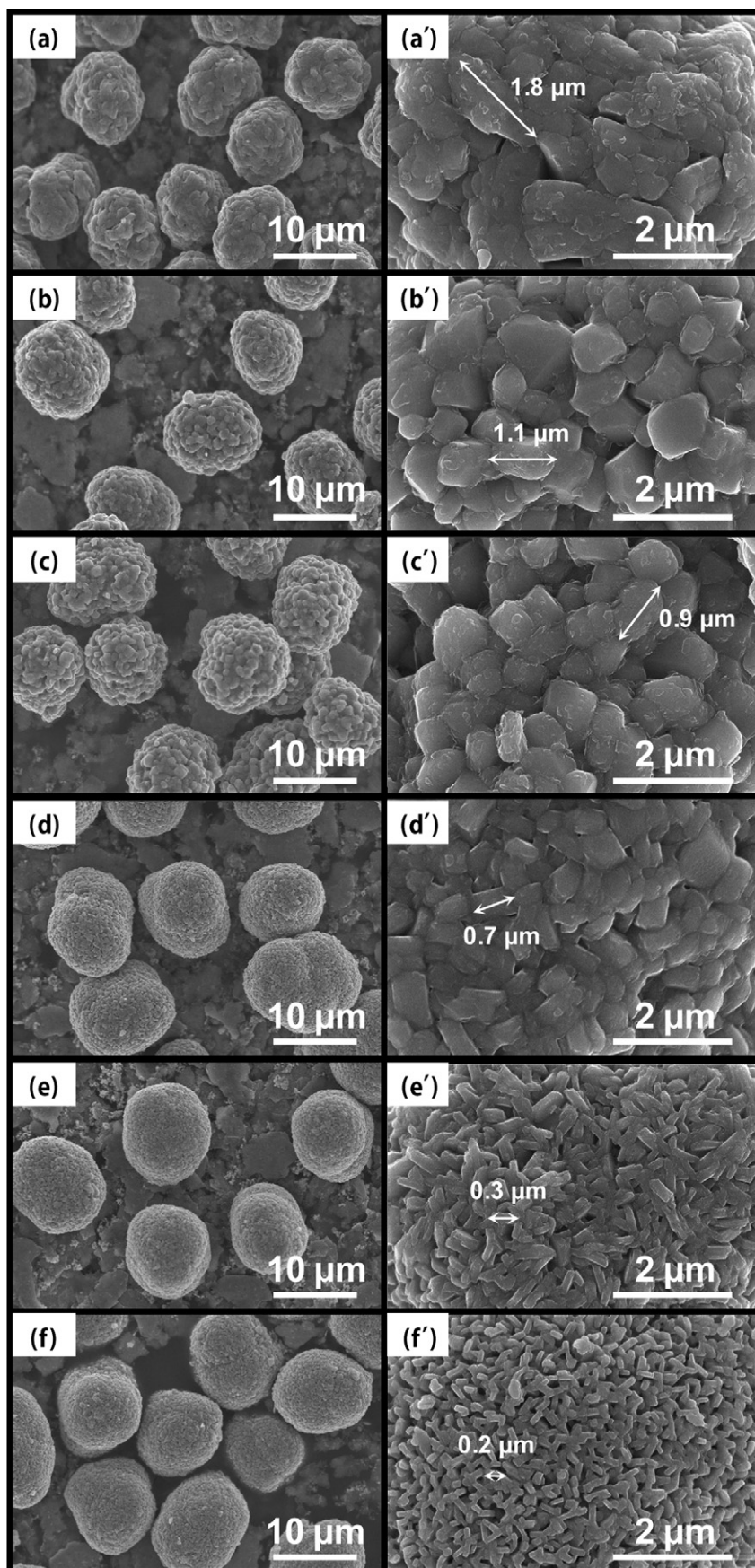
Fig. 2. SEM images of as-prepared Li[Ni$_x$Co$_y$Mn$_z$]O$_2$ powders: (a) $x = 1/3$, (b) $x = 0.5$, (c) $x = 0.6$, (d) $x = 0.7$, (e) $x = 0.8$ and (f) $x = 0.85$ where ′ indicates the magnified images of the corresponding samples.

Table 2
Total residual lithium amounts (LiOH and Li_2CO_3) on the $Li[Ni_xCo_yMn_z]O_2$ cathode surface. (unit: ppm).

	LiOH	Li_2CO_3	Total
$Li[Ni_{1/3}Co_{1/3}Mn_{1/3}]O_2$	790	1008	1798
$Li[Ni_{0.5}Co_{0.2}Mn_{0.3}]O_2$	1316	1080	2396
$Li[Ni_{0.6}Co_{0.2}Mn_{0.2}]O_2$	2593	2315	4908
$Li[Ni_{0.7}Co_{0.15}Mn_{0.15}]O_2$	4514	6540	11,054
$Li[Ni_{0.8}Co_{0.1}Mn_{0.1}]O_2$	10,996	12,823	23,819
$Li[Ni_{0.85}Co_{0.075}Mn_{0.075}]O_2$	11,285	15,257	26,542

appeared smooth after cycling. Phase identification using selected area electron diffraction (ED) of the primary particles on the surface revealed that most of the examined surface particles (~90%) possessed a spinel-like structure. A typical ED pattern in the 001 zone of the cubic structure shown in Fig. 6b clearly verified the existence of a cubic phase in the cycled $Li[Ni_{0.85}Co_{0.075}Mn_{0.075}]O_2$ electrode as the 4-fold symmetry apparent in Fig. 6b is not possible in the original layered structure. In addition, the structure of primary particles located in the interior of a spherical secondary particle was also examined by looking for the particles that have

been split apart during cycling. ED analysis of such particles suggested that the primary particle in the interior mostly retained the initial layered structure. From the ED data, it is likely that the main reason for the inferior Li^+ intercalation stability of the $Li[Ni_{0.85}Co_{0.075}Mn_{0.075}]O_2$ can be traced to the structural degradation of the primary particles on the surface from the layered structure to a spinel-like structure. In fact, development of a NiO-like (also with the cubic symmetry) structure on the surface of the $Li[Ni_{0.8}Co_{0.2}]O_2$ cathode is believed to be linked to the rise in the charge transfer resistance and eventual deterioration of the cell efficiency [23,24]. On the other hand, the tendency for the surface primary particle to transform to a spinel-like structure was considerably reduced for the $Li[Ni_{0.6}Co_{0.2}Mn_{0.2}]O_2$ cathode which showed much improved capacity retention after 100 cycles at 55 °C. The primary particles from the cycled $Li[Ni_{0.6}Co_{0.2}Mn_{0.2}]O_2$ electrode were much larger (~1 μm in size) compared to those of $Li[Ni_{0.85}Co_{0.075}Mn_{0.075}]O$ as can be seen from the bright field TEM image of the cycled $Li[Ni_{0.6}Co_{0.2}Mn_{0.2}]O_2$ electrode in Fig. 6c. Most of the observed particles from this electrode were identified as the layered structure whose example is shown in Fig. 6d. The ED pattern in Fig. 6d was unequivocally indexed to the 100 zone of the
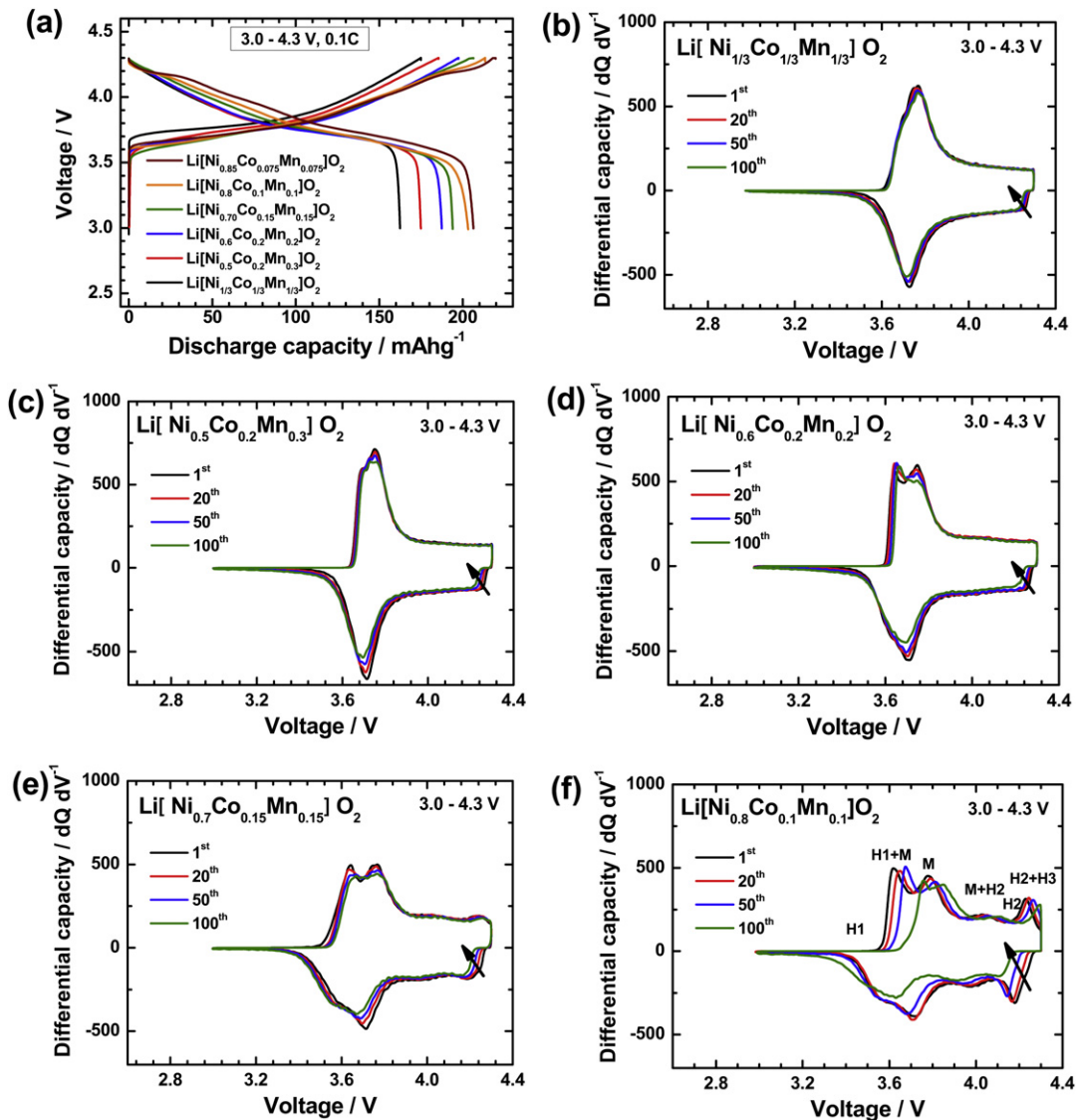
Fig. 3. (a) Initial charge–discharge curves of $Li/Li[Ni_xCo_yMn_z]O_2$ ($x = 1/3$, 0.5, 0.6, 0.7, 0.8 and 0.85) and corresponding differential capacity vs. voltage curves for (b) $x = 1/3$, (c) $x = 0.5$, (d) $x = 0.6$, (e) $x = 0.7$ and (f) $x = 0.8$. The applied current density across the positive electrode was 20 mA g^{-1} (0.1 C) at 25 °C in the voltage range of 3.0–4.3 V.
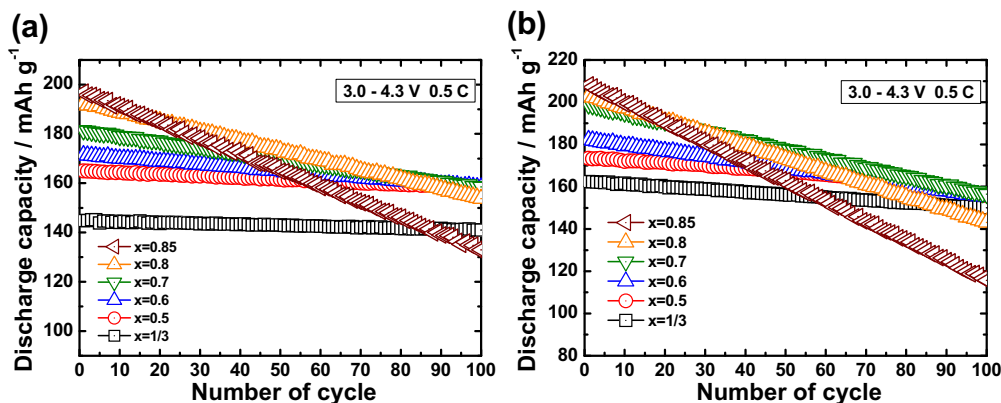
Fig. 4. Discharge capacity vs. cycle number for the Li/Li[Ni$_x$Co$_y$Mn$_z$]O$_2$ (x = 1/3, 0.5, 0.6, 0.7, 0.8 and 0.85) cells at (a) 25 °C and (b) 55 °C. The applied current density across the positive electrode was 100 mA g^{-1} (0.5 C) in the voltage range of 3.0–4.3 V.

layered structure; however, occasionally a primary particle with a spinel-like structure was also found for the cycled Li[Ni$_{0.6}$Co$_{0.2}$Mn$_{0.2}$]O$_2$ electrode. The Li[Ni$_{1/3}$Co$_{1/3}$Mn$_{1/3}$]O$_2$ cathode which exhibited the best Li$^+$ intercalation stability had extremely large primary particles whose size was difficult to estimate as can be from the bright field TEM image of the cycled Li[Ni$_{1/3}$Co$_{1/3}$Mn$_{1/3}$]O$_2$ electrode shown in Fig. 6e. In spite of the large particle size, the primary particles remained intact after 100 cycles and also retained the original layered rhombohedral structure as verified by the ED pattern indexed again to the 100 zone of the rhombohedral layered structure shown in Fig. 6f. In spite of the small sampling population (10–20 particles for each composition) examined by

TEM, there was a qualitative trend in the degree of the structural degradation especially on the cathode particle surface with the increasing Ni concentration. Increasing Ni content appears to favor the spinel-like transformation of the primary particles, leading to the gradual deterioration of the discharge capacity. It is also noted that the particle size which almost proportionally decreased with the Ni content may have also contributed to the structural stability of the Li[Ni$_{1/3}$Co$_{1/3}$Mn$_{1/3}$]O$_2$ electrode. It is expected that the large particles would be more difficult to undergo a structural transformation due to the strain associated with the transformation than the smaller particles would.

The rate capability test results of the Li[Ni$_x$Co$_y$Mn$_z$]O$_2$ (x = 1/3, 0.5, 0.6, 0.7, 0.8 and 0.85) cells are shown in Fig. 7. Each cell was charged galvanostatically at a 0.2 C-rate (40 mA g^{-1}) before each discharge test and then discharged at different C-rates ranging from 0.2 to 5 C (40–1000 mA g^{-1}). As can be seen in Fig. 7, the rate capability of Li[Ni$_x$Co$_y$Mn$_z$]O$_2$ gradually improved with increasing Ni content (x). For example, the capacity retention of Li[Ni$_{1/3}$Co$_{1/3}$Mn$_{1/3}$]O$_2$ at 5 C compared to 0.2 C was 75.1%, while Li[Ni$_{0.85}$Co$_{0.075}$Mn$_{0.075}$]O$_2$ exhibited a much enhanced capacity retention of 90%.

In order to study the contribution of the electronic conductivity and chemical Li$^+$ diffusivity on the rate capability, we measured the electronic conductivities of Li[Ni$_x$Co$_y$Mn$_z$]O$_2$ (x = 1/3, 0.5, 0.6, 0.7, 0.8 and 0.85) by a four probe method and the results are shown in Table 3. The electronic conductivity linearly increased with increasing Ni content (x). The electronic conductivity for the Li[Ni$_{0.85}$Co$_{0.075}$Mn$_{0.075}$]O$_2$ material is high (2.8 × 10^{-5} S cm^{-1}), which was greatly increased by three orders of magnitude compared to Li[Ni$_{1/3}$Co$_{1/3}$Mn$_{1/3}$]O$_2$ (5.2 × 10^{-8} S cm^{-1}). We believe that the increase of the electronic conductivity with increasing Ni content is due to the Ni^{2+}/Ni^{3+} mixed valence effect because the Ni^{3+} concentration increases with increasing Ni content in Li[Ni$_x$Co$_y$Mn$_z$]O$_2$ (x = 1/3, 0.5, 0.6, 0.7, 0.8 and 0.85) [8]. As a cross-validation, the chemical Li$^+$ diffusivities for Li[Ni$_x$Co$_y$Mn$_z$]O$_2$ (x = 1/3, 0.5, 0.6, 0.7 and 0.8) were measured by the galvanostatic intermittent titration technique (GITT) [18]. As can be seen in Fig. 8, the Li$^+$ diffusivity increased with increasing Ni content (x) in which the Li$^+$ diffusivity ranged from 10^{-12} to 10^{-8} cm^2 S^{-1}. The Li$^+$ diffusivity for Li[Ni$_{0.8}$Co$_{0.1}$Mn$_{0.1}$]O$_2$ was ∼10^3 times higher (10^{-8}–10^{-9} cm^2 S^{-1}) than the value for Li[Ni$_{1/3}$Co$_{1/3}$Mn$_{1/3}$]O$_2$ (10^{-11} cm^2 S^{-1}). The chemical Li$^+$ diffusivity decreased to a minima up to δ = 0.4 for Li$_{1-\delta}$[Ni$_x$Co$_y$Mn$_z$]O$_2$ (x = 0.5, 0.6, 0.7, 0.8 and 0.85) upon the beginning of Li$^+$ deintercalation before it increased and showed two maxima around δ = 0.65 and δ = 0.9. The minima of the Li$^+$ diffusivity on charging are well matched with the CV maxima around 3.65 V (Fig. 3b–f) and with the charging voltage plateau
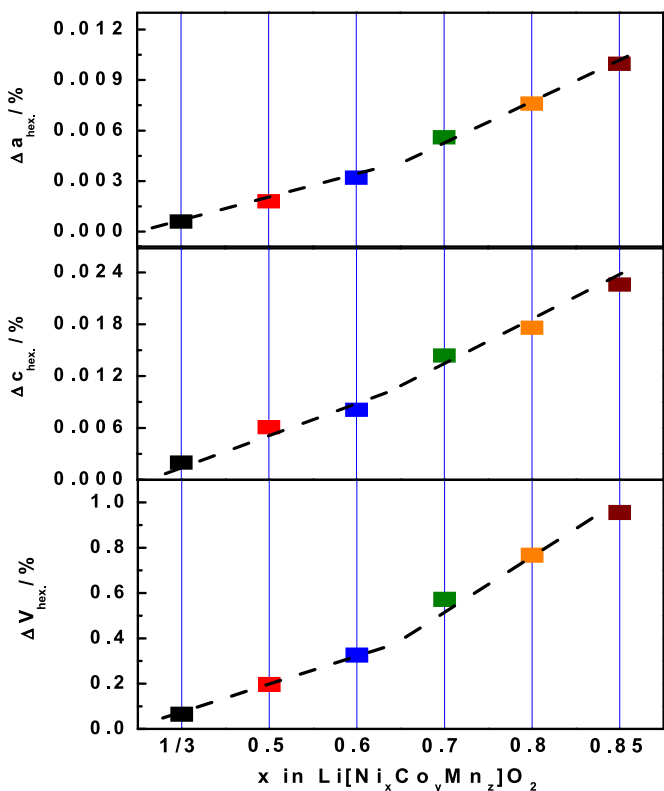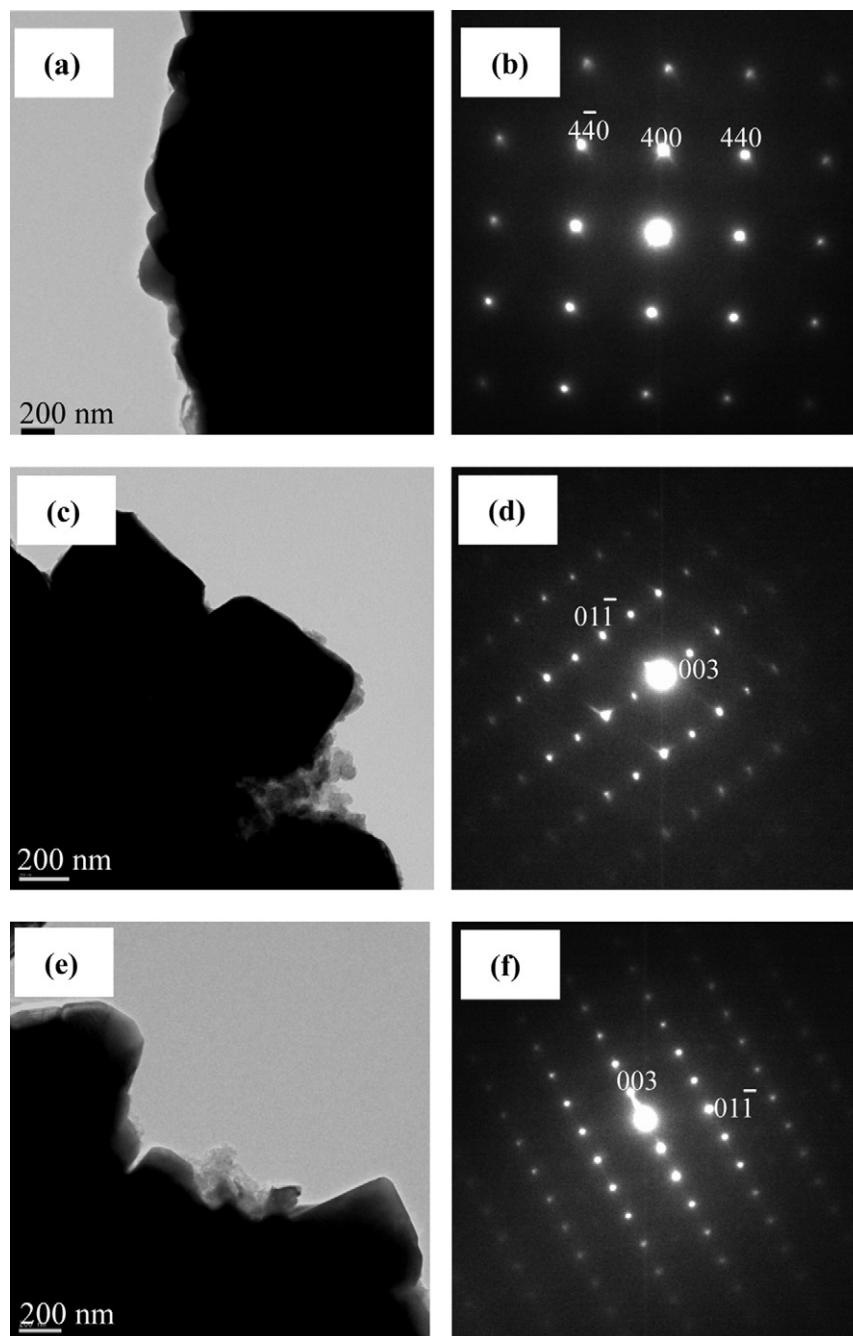

Fig. 5. Variation of the lattice parameters (a and c) and volume of Li[Ni$_x$Co$_y$Mn$_z$]O$_2$ (x = 1/3, 0.5, 0.6, 0.7, 0.8 and 0.85) after 100 cycles at the upper cutoff voltage of 4.3 V at 25 °C.

Fig. 6. TEM images and electron diffraction patterns from the Li[Ni$_x$Co$_{0.5-x/2}$Mn$_{0.5-x/2}$]O$_2$ electrode after 100 cycles with the upper cutoff voltage of 4.3 V at 55 °C: (a)–(b) $x = 0.85$, (c)–(d) $x = 0.6$ and (e)–(f) $x = 1/3$.

(Fig. 3a) during the first charging [25]. Similar Li$^+$ diffusivity behavior as a function of the Li$^+$ amount was previously reported and was related to phase transition [26–29]. From the above results, we believe that the high rate capability of Li[Ni$_x$Co$_y$Mn$_z$]O$_2$ ($x = 1/3$, 0.5, 0.6, 0.7, 0.8 and 0.85) is strongly correlated with both the electronic conductivity and chemical Li$^+$ diffusivity.

To evaluate the differences of the safety characteristics of the Li[Ni$_x$Co$_y$Mn$_z$]O$_2$ ($x = 1/3$, 0.5, 0.6, 0.7, 0.8 and 0.85) materials, we measured the oxygen release from chemically delithiated Li$_{1-\delta}$[Ni$_x$Co$_y$Mn$_z$]O$_2$ by thermal gravimetric analysis (TGA). Fig. 9 shows the TGA curves of Li$_{1-\delta}$[Ni$_x$Co$_y$Mn$_z$]O$_2$ ($x = 1/3$, 0.5, 0.6, 0.7, 0.8 and 0.85) recorded between room temperature and 600 °C under flowing purified air. Three distinct features were observed

for all of the Li$_{1-\delta}$[Ni$_x$Co$_y$Mn$_z$]O$_2$ ($x = 1/3$, 0.5, 0.6, 0.7, 0.8 and 0.85) materials with first, second, and third weight losses attributed to oxygen release as a result of several phase transitions from a layered ($R\overline{3}m$) → M$_3$O$_4$ spinel ($Fd\overline{3}m$) to M$_3$O$_4$ spinel ($Fd\overline{3}m$) → NiO rock-salt ($Fm3m$) [30–33]. The phase transition temperature shifted to lower temperatures with increasing Ni content due to the decreased structural stability. Note that the total amount of oxygen release also increased with increasing Ni content from 18.4% for Li$_{0.27}$(Ni$_{1/3}$Co$_{1/3}$Mn$_{1/3}$)O$_2$ to 51.7% for Li$_{0.21}$[Ni$_{0.85}$Co$_{0.075}$Mn$_{0.075}$]O$_2$. The stability of the delithiated Li$_{1-\delta}$[Ni$_x$Co$_y$Mn$_z$]O$_2$ ($x = 1/3$, 0.5, 0.6, 0.7, 0.8 and 0.85) decreased because unstable and reactive Ni^{4+} ions transformed to more stable Ni^{2+} by moving from the octahedral sites into tetrahedral sites, concurrently accompanied by
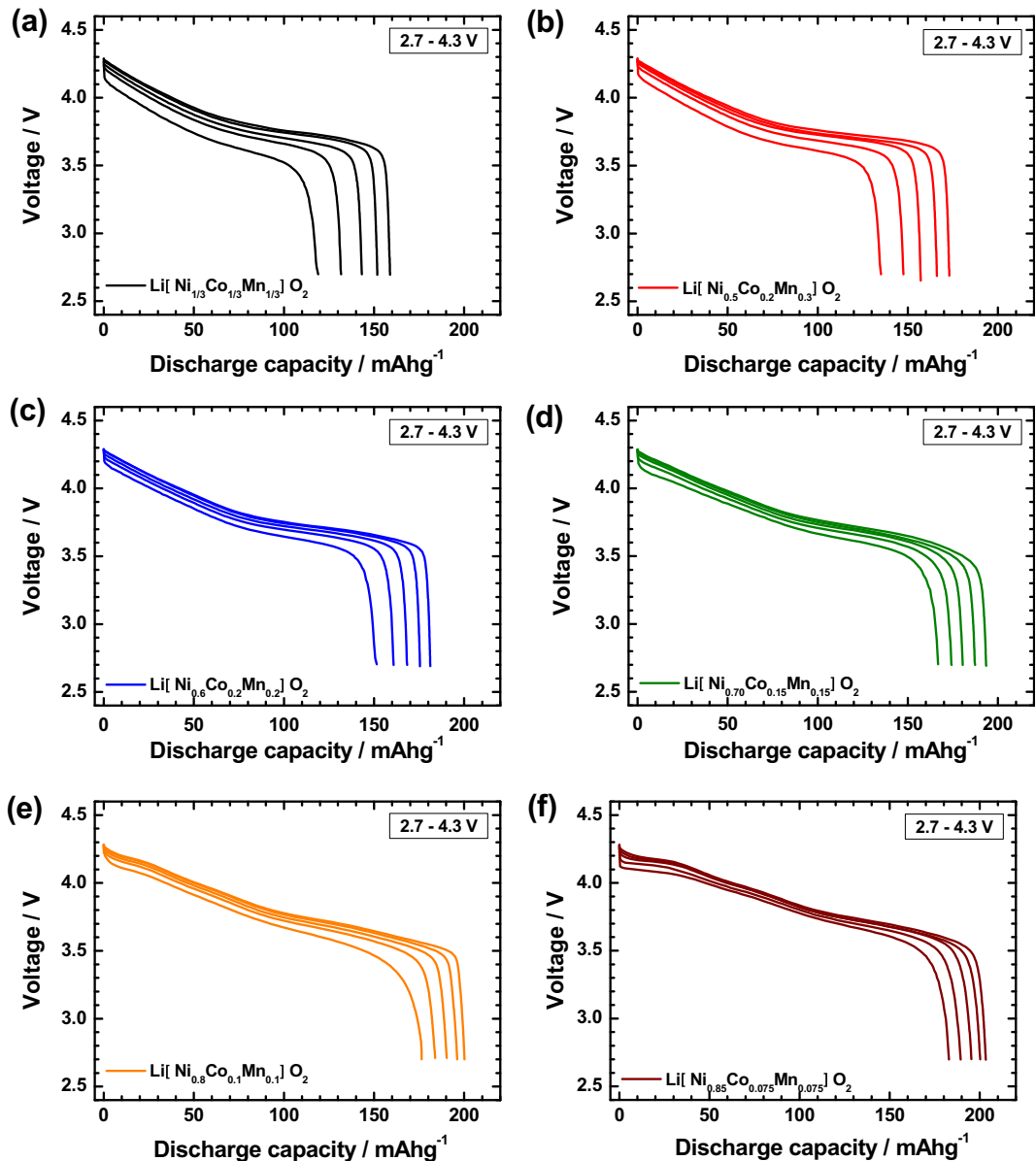
Fig. 7. Discharge curves of the Li/Li[$Ni_xCo_yMn_z$]O_2 cells with (a) x = 1/3, (b) x = 0.5, (c) x = 0.6, (d) x = 0.7, (e) x = 0.8 and (f) x = 0.85 as a function of the C-rates.

oxygen release. In addition, the formed spinel M_3O_4 with a high Ni content from layers is very unstable due to the mixture of unstable Ni^{3+} and Ni^{4+} such that phase transition to rock-salt NiO is likely to occur. Recently, Belharouak et al. [34] reported that chemically delithiated $Li_{0.45}(Ni_{0.8}Co_{0.15}Al_{0.05})O_2$ or $Li_{0.55}(Ni_{1/3}Co_{1/3}Mn_{1/3})O_2$ powders have different tendencies to release oxygen because $Li_{0.55}(Ni_{1/3}Co_{1/3}Mn_{1/3})O_2$ suffered from less structural disorder due to the formation of a stable spinel phase during the thermal

Table 3
Electronic conductivity of the Li[$Ni_xCo_yMn_z$]O_2 (x = 1/3, 0.5, 0.6, 0.7, 0.8 and 0.85).

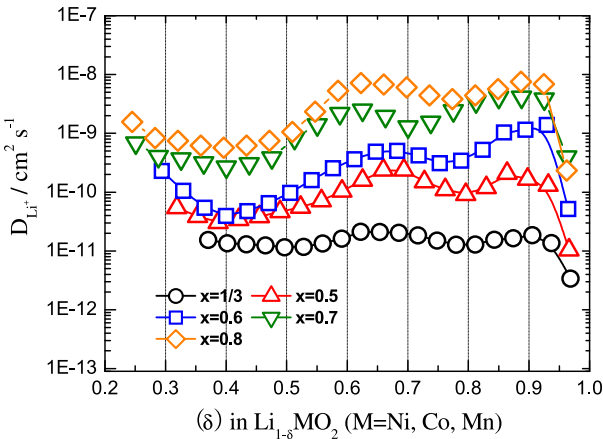|	Electronic conductivity (S cm^{-1})
Li[$Ni_{1/3}Co_{1/3}Mn_{1/3}$]O_2	5.2×10^{-8}
Li[$Ni_{0.5}Co_{0.2}Mn_{0.3}$]O_2	4.9×10^{-7}
Li[$Ni_{0.6}Co_{0.2}Mn_{0.2}$]O_2	1.6×10^{-6}
Li[$Ni_{0.7}Co_{0.15}Mn_{0.15}$]$O_2$	9.3×10^{-6}
Li[$Ni_{0.8}Co_{0.1}Mn_{0.1}$]O_2	1.7×10^{-5}
Li[$Ni_{0.85}Co_{0.075}Mn_{0.075}$]$O_2$	2.8×10^{-5}

Fig. 8. Variation of the chemical diffusion coefficient, DLi^+, of Li[$Ni_xCo_yMn_z$]O_2 (x = 1/3, 0.5, 0.6, 0.7 and 0.8) as a function of the state of charge.
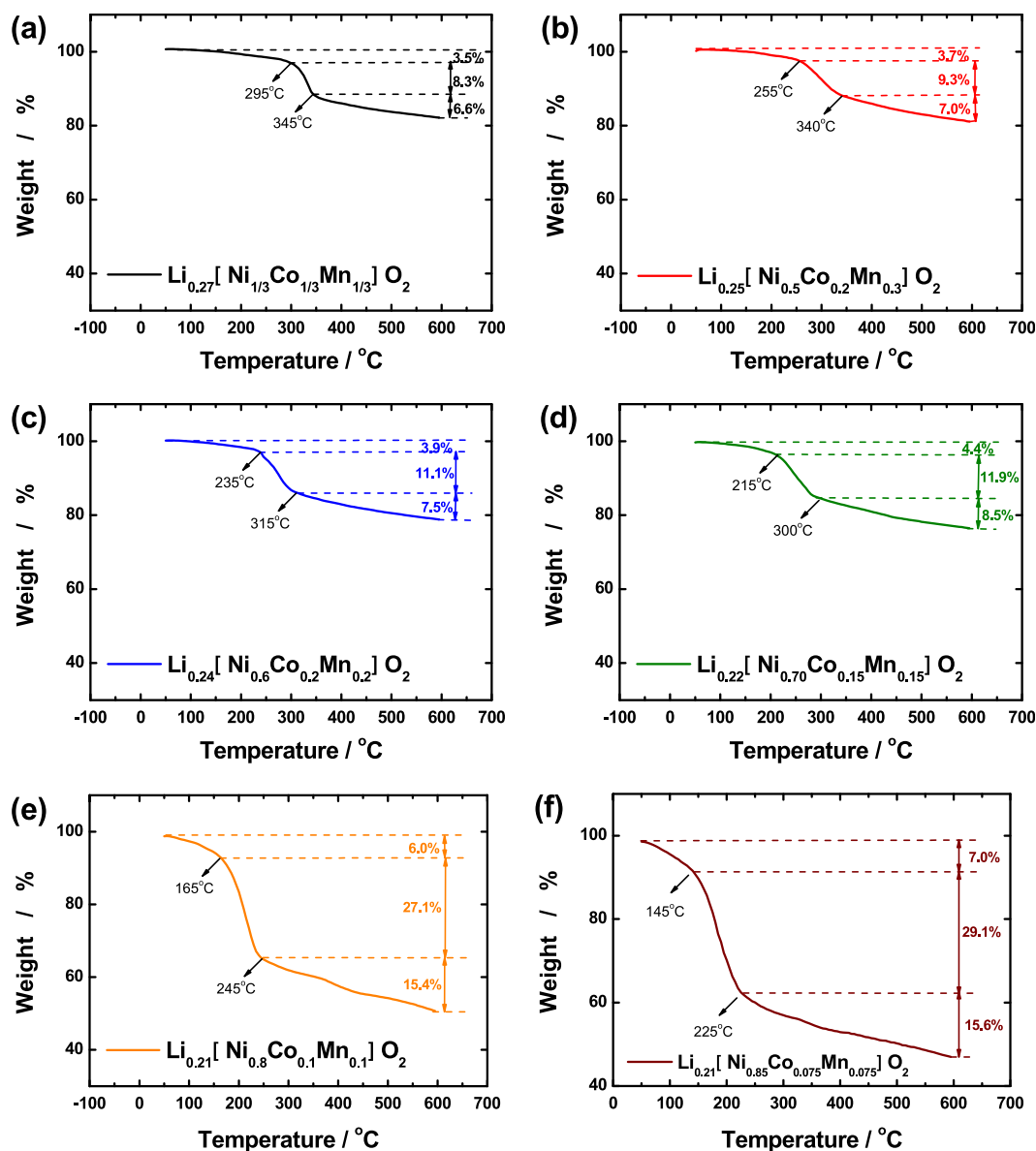
Fig. 9. TGA curves of the chemically delithiated $Li_{1-\delta}[Ni_xCo_yMn_z]O_2$ with (a) $x = 1/3$, (b) $x = 0.5$, (c) $x = 0.6$, (d) $x = 0.7$, (e) $x = 0.8$ and (f) $x = 0.85$.

processes while $Li_{0.45}(Ni_{0.8}Co_{0.15}Al_{0.05})O_2$ experienced the formation of a thermodynamically unstable spinel phase leading to more oxygen release to form a NiO-type phase.

The thermal stabilities of electrochemically delithiated wet Li $[Ni_xCo_yMn_z]O_2$ ($x = 1/3$, 0.5, 0.6, 0.7, 0.8 and 0.85) electrodes were evaluated by differential scanning calorimetry (DSC). As can be seen in Fig. 10, the exothermic reaction peak temperature gradually shifted to lower temperatures accompanied with higher heat generation as the Ni content increased: 306 °C and 512.5 J g^{-1} for $Li_{0.37}[Ni_{1/3}Co_{1/3}Mn_{1/3}]O_2$, 290 °C and 605.7 J g^{-1} for $Li_{0.34}[Ni_{0.5}Co_{0.2}Mn_{0.3}]O_2$, 260 °C and 721.4 J g^{-1} for $Li_{0.30}[Ni_{0.6}Co_{0.2}Mn_{0.2}]O_2$, 242 °C and 826.3 J g^{-1} for $Li_{0.26}[Ni_{0.70}Co_{0.15}Mn_{0.15}]O_2$, 232 °C with 971.5 J g^{-1} for $Li_{0.23}[Ni_{0.8}Co_{0.1}Mn_{0.1}]O_2$ and 225 °C and 971.5 J g^{-1} for $Li_{0.21}[Ni_{0.85}Co_{0.075}Mn_{0.075}]O_2$. We believe that the improved thermal stability of $Li[Ni_xCo_yMn_z]O_2$ with lower Ni contents can be ascribed to the increased stable Mn^{4+} and reduced reactive Ni^+ contents, as explained previously, resulting in suppression of the increased charge transfer resistance [35]. Notably, the exothermic peak temperature decreased by a larger extent from a Ni content (x)
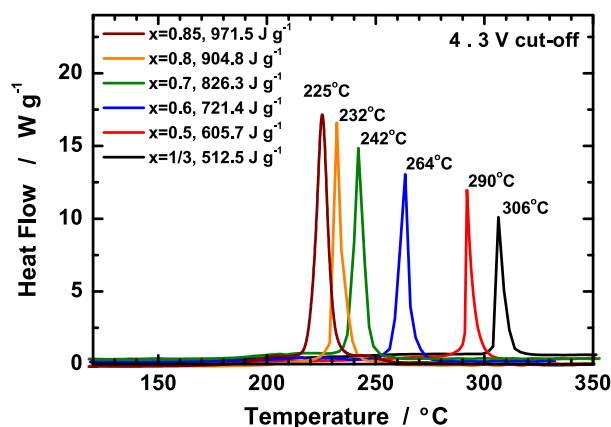

Fig. 10. DSC results of the $Li_{1-\delta}[Ni_xCo_yMn_z]O_2$ materials ($x = 1/3$, 0.5, 0.6, 0.7, 0.8 and 0.85).
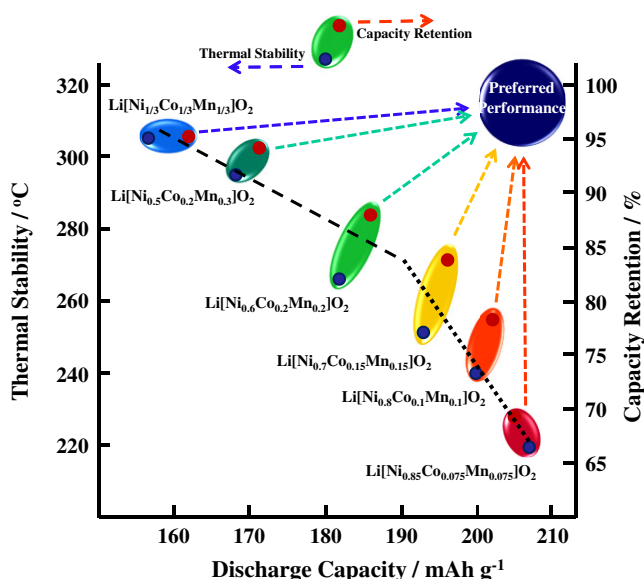
Fig. 11. A map of relationship between discharge capacity, and thermal stability and capacity retention of $Li/Li[Ni_xCo_yMn_z]O_2$ (x = 1/3, 0.5, 0.6, 0.7, 0.8 and 0.85).

of 0.5–0.6 indicating that $Li[Ni_xCo_yMn_z]O_2$ materials with x values greater than 0.6 have poor thermal stabilities for use in commercial cells.

As summarized in Fig. 11, the 1/3 cathode exhibited the best capacity retention and thermal stability among the tested compositions; however, its discharge capacity was limited due to the least amount of Ni in the composition. On the other hand, the 0.85 cathode which contained the highest Ni content experienced severe capacity fading. The capacity fading mechanism is believed to be the overall volume expansion of the electrode during cycling as attested by XRD and the surface structural degradation (transformation to the spinel-like structure) as confirmed by TEM. In addition, the 0.85 electrode exhibited the worst thermal stability in spite of the large discharge capacity while the 1/3 electrode showed the highest safety. Hence, as can be indicated Fig. 10, the composition and microstructure of the $Li[Ni_xCo_yMn_z]O_2$ needs to be further optimized to attain an ideal cathode material with high capacity and thermal stability.

4. Conclusions

To determine the optimal composition of $Li[Ni_xCo_yMn_z]O_2$ (x = 1/3, 0.5, 0.6, 0.7, 0.8 and 0.85), the electrochemical and thermal properties are investigated as a function of the Ni content. It is found that the electrochemical properties and safety strongly depend on the microstructure (particle morphology and surface/bulk structural stability) and the physico-chemical properties (Li^+ diffusivity, electronic conductivity, volume expansion, chemical stability, and excess lithium). There is an nearly linear decrease in the thermal stability and capacity retention as the discharge capacity is raised by increasing the relative fraction of Ni in the $Li[Ni_xCo_yMn_z]O_2$ electrodes. However, as indicated by the change of the slope in Fig. 11, although increasing the relative fraction of Ni still raises the discharge capacity beyond $Li[Ni_{0.6}Co_{0.2}Mn_{0.2}]O_2$, the thermal stability deteriorates at a faster rate so that the advantage gained by the increased discharge capacity is quickly negated by the concurrent deterioration of the battery safety. The faster decrease in the thermal stability is related to the increasing structural instability of the electrodes upon Li deintercalation beyond $Li[Ni_{0.6}Co_{0.2}Mn_{0.2}]O_2$ as observed in Fig. 5. It

appears that it would not be possible to develop an ideal cathode material that possesses both high capacity and high safety just by changing the composition. Hence, it is suggested that the composition of $Li[Ni_xCo_yMn_z]O_2$ has to be selectively designed based on the required application. Alternatively, a core–shell (or with concentration gradient) [2,4] or full concentration gradient cathode materials [33,36] consisting of an outer shell with high Mn content providing the required thermal stability and an inner core with high Ni content generating a high discharge capacity can be developed to attain an optimal performance from the layer-structured $Li[Ni_xCo_yMn_z]O_2$ cathode materials.

References

[1] A.K. Padhi, K.S. Nanjundaswamy, J.B. Goodenough, J. Electrochem. Soc. 144 (1997) 1188–1194.
[2] Y.-K. Sun, S.-T. Myung, B.-C. Park, J. Prakash, I. Belharouak, K. Amine, Nat. Mater. 8 (2009) 320–324.
[3] N. Recham, J.-N. Chotard, L. Dupont, C. Delacourt, W. Walker, M. Armand, J.-M. Tarascon, Nat. Mater. 9 (2010) 68–74.
[4] Y.-K. Sun, S.-T. Myung, M.-H. Lee, J. Prakash, K. Amine, J. Am. Chem. Soc. 127 (2005) 13411–13418.
[5] T. Ohzuku, Y. Makimura, Chem. Lett. 30 (2001) 642–643.
[6] T. Ohzuku, Y. Makimura, Chem. Lett. 30 (2001) 744–745.
[7] J. Katana Ngala, Natasha A. Chernova, M. Ma, M. Mamak, P.Y. Zavalij, M.S. Whittingham, J. Mater. Chem. 14 (2004) 214–220.
[8] K. Shizuka, T. Kobayashi, K. Okahara, K. Okamoto, S. Kanzaki, R. Kanno, J. Power Sources 146 (2005) 589–593.
[9] S.W. Oh, S.-H. Park, K. Amine, Y.-K. Sun, J. Power Sources 160 (2006) 558–562.
[10] K.-S. Lee, S.-T. Myung, K. Amine, H. Yashiro, Y.-K. Sun, J. Electrochem. Soc. 154 (2007) A971–A977.
[11] M.-H. Kim, H.-S. Shin, D. Shin, Yang-Kook Sun, J. Power Sources 159 (2006) 1328–1333.
[12] Y.S. Park, K.-H. Choi, H.-K. Park, S.-M. Lee, J. Electrochem. Soc. 157 (2010) A850–A853.
[13] P.Y. Liao, J.G. Duh, S.R. Sheen, J. Electrochem. Soc. 152 (2005) A1695–A1700.
[14] J. Li, L. Wang, Q. Zhang, X. He, J. Power Sources 189 (2009) 28–33.
[15] I. Belharouak, Y.-K. Sun, J. Liu, K. Amine, J. Power Sources 123 (2003) 247–252.
[16] M.-H. Lee, Y.-J. Kang, S.-T. Myung, Y.-K. Sun, Electrochim. Acta 50 (2004) 939–948.
[17] R.D. Shannon, Acta Cryst. A32 (1976) 751–767.
[18] K. Matsumoto, R. Kuzuo, K. Takeya, A. Yamanaka, J. Power Sources 81–82 (1999) 558–561.
[19] M. Noh, Y. Lee, J. Cho, J. Electrochem. Soc. 153 (2006) A935–A940.
[20] J. Eom, M.G. Kim, J. Cho, J. Electrochem. Soc. 155 (2008) A239–A245.
[21] W. Li, J.N. Reimers, J.R. Dahn, Solid State Ionics 67 (1993) 123–130.
[22] S.-U. Woo, C.S. Yoon, K. Amine, I. Belharouak, Y.-K. Sun, J. Electrochem. Soc. 154 (2007) A1005–A1009.
[23] D.P. Abraham, R.D. Twesten, M. Balasubramanian, I. Petrov, J. McBreen, K. Amine, Electrochem. Commun. 4 (2002) 620–625.
[24] A.M. Andersson, D.P. Abraham, R. Haasch, S. MacLaren, J. Liu, K. Amine, J. Electrochem. Soc. 149 (2002) A1358–A1369.
[25] K.M. Shaju, G.V. Subba Rao, B.V.R. Chowdari, Electrochim. Acta 49 (2004) 1565–1576.
[26] K.M. Shaju, G.V. Subba Rao, B.V.R. Chowdari, J. Electrochem. Soc. 151 (2004) A1324–A1332.
[27] K.M. Shaju, G.V. Subba Rao, B.V.R. Chowdari, J. Mater. Chem. 13 (2003) 106–133.
[28] J.-S. Hong, J.R. Selman, J. Electrochem. Soc. 147 (2000) 3190–3194.
[29] Y.-I. Jang, B.J. Neudecker, N.J. Dudney, Electrochem. Solid-State Lett. 4 (2001) A74–A77.
[30] M. Guilmard, L. Croguennec, C. Delmas, Chem. Mater. 15 (2003) 4484–4493.
[31] L. Wu, K.-W. Nam, X. Wang, Y. Zhou, J.-C. Zheng, X.-Q. Yang, Y. Zhu, Chem. Mater. 23 (2011) 3953–3960.
[32] H. Konishi, T. Yuasa, M. Yoshikawa, J. Power Sources 196 (2011) 6884–6888.
[33] H.-J. Noh, S.-T. Myung, H.-G. Jung, H. Yashiro, K. Amine, Y.-K. Sun, Adv. Funct. Mater. (2012). http://dx.doi.org/10.1002/adfm.201200699.
[34] I. Belharouak, W. Lu, D. Vissers, K. Amine, Electrochem. Commun. 8 (2006) 329–335.
[35] Y.-K. Sun, H.-J. Noh, C.S. Yoon, J. Electrochem. Soc. 159 (2012) A1–A5.
[36] Y.-K. Sun, Z. Chen, H.-J. Noh, D.-J. lee, H.-G. Jung, Y. Ren, S. Wang, C.S. Yoon, S.-T. Myung, K. Amine, Nat. Mater. 11 (2012) 942–947.